

Temperature-dependent performance of silicon heterojunction solar cells with transition-metal-oxide-based selective contacts

Anh Huy Tuan Le¹  | Julie Dréon² | Jesús Ibarra Michel³ | Mathieu Boccard² | James Bullock³ | Nino Borojevic¹ | Ziv Hameiri¹

¹School of Photovoltaic and Renewable Energy Engineering, University of New South Wales, Sydney, New South Wales, Australia

²Photovoltaics and Thin-Film Electronics Laboratory (PV-lab), Institute of Microengineering (IMT), École Polytechnique Fédérale de Lausanne (EPFL), Neuchâtel, Switzerland

³Department of Electrical and Electronic Engineering, University of Melbourne, Melbourne, Victoria, Australia

Correspondence

Anh Huy Tuan Le, School of Photovoltaic and Renewable Energy Engineering, University of New South Wales, Sydney, NSW 2052, Australia.

Email: leanh619@gmail.com

Funding information

Swiss National Science Foundation, Grant/Award Number: PZENP2_173627; Australian Renewable Energy Agency, Grant/Award Number: 2017/RND001

Abstract

The temperature coefficient (TC) is an essential figure of merit to accurately evaluate solar cell performance at various operating temperatures and hence enabling the comparison between different cell technologies. Recently, solar cells that use passivating contacts based on transition metal oxide (TMO) layers have attracted much attention due to their excellent performance. Therefore, knowledge of their TCs and insights into their performance at various operating temperatures are of significant interest. In this study, we investigate the temperature-dependent performance of solar cells with TMO-based passivating contacts at various illumination intensities. We then compare their performance to that of standard silicon heterojunction (SHJ) solar cells. The efficiency TC (TC_{η}) of solar cells that use passivating contacts based on molybdenum oxide (MoO_x) and titanium oxide (TiO_x) films is found to be almost identical. Both outperform the TC_{η} of the standard SHJ cells and are greatly superior to those of cell structures without passivating contacts. The superior TC_{η} of the MoO_x -based cells is mainly due to their favourable TCs of the short-circuit current density (TC_{Jsc}) and fill factor (TC_{FF}), whereas the superiority of TC_{η} of the TiO_x -based cells is solely resulting from the superior TC_{FF} . The favourable TC_{Jsc} of the MoO_x -based cells is explained by an enhanced spectral response at short wavelengths with increasing temperature, due to the improvement of the passivation quality of the MoO_x -based passivating contacts. The beneficial TC_{FF} of both solar cells is partly resulting from the improvement of the contact resistivity of the TMO-based passivating contacts which counterbalances some of the fill factor losses at elevated temperatures. Although an improvement of the passivation quality of the TMO-based passivating contacts is observed at elevated temperature, it does not have a strong impact on the TC of the open-circuit voltage of the investigated solar cells. Furthermore, we also found that the studied cells are less sensitive to temperature variation at higher illumination intensities.

KEY WORDS

MoO_x , passivating contacts, SHJ, silicon solar cells, temperature coefficient, temperature dependence, TiO_x , TMO

1 | INTRODUCTION

Photovoltaic (PV) devices operate under a wide range of temperatures¹; however, they are often characterized and optimized only at standard testing conditions (STCs; at 25°C with an irradiance of 1000 W/m² under the AM1.5G solar spectrum). Since the temperature sensitivity of various cell technologies is different,² the temperature coefficient (TC) is an essential figure of merit to evaluate the cell performance at different operating temperatures and to allow a more in-depth comparison between various cell technologies.^{2–4} More importantly, in combination with the typical meteorological data, this parameter enables to accurately evaluate the energy yield of PV installations. Hence, it plays a crucial role in the selection of suitable cell technologies for a PV field at a specific site to maximize the annual energy yield. The performance of silicon (Si) solar cells is typically reduced with increasing temperature, which is mainly attributed to the reduction of the cell's open-circuit voltage (V_{oc}).⁵ In general, the higher the cell's V_{oc} , the better the open-circuit voltage TC (TC _{V_{oc}}), and hence, the efficiency TC (TC _{η}).⁵ To achieve a favourable TC _{η} , cell structures enabling a high V_{oc} are therefore desired.⁵

Recent studies have demonstrated the capability of solar cells that integrate passivating contacts to achieve high efficiencies.^{6–11} Such contacts are typically composed of three layers: (1) films that provide surface passivation, (2) films that ensure carrier selectivity and (3) metal (or degenerately doped transparent conductive oxide) electrodes that ensure electrical connection to the external circuit. Only in rare cases, one layer is sufficient for all three tasks,¹² whereas, in most of the cases, layers (2) and (3) both play a role in selectivity and can also contribute to passivation.^{13–17} Efficient passivating contacts minimize the recombination losses at the Si interfaces and ensure an effective collection of only one type of charge carrier.^{13–15} Cell structures that integrate these contacts usually exhibit a high V_{oc} ,^{9,18–21} and hence, they are expected to have a favourable TC _{η} . This was confirmed by our recent study demonstrating that the TC _{η} of solar cells with polysilicon passivating contacts is superior to those of cell structures without passivating contacts (such as passivated emitter and rear contact [PERC], passivated emitter rear totally diffused [PERT] and more).^{22,23} It highlights the advantage of using solar cells that integrate passivating contacts in the field.

Besides polysilicon passivating contacts, passivating contacts based on transition metal oxide (TMO) films have also attracted much attention due to their excellent performance.^{10,11} Depending on the electrical properties (such as work function, conductivity and band alignment), these contacts can be used as hole- or electron-selective collectors.¹⁵ For examples, for hole-selective contacts, molybdenum oxide (MoO_x),^{11,24} vanadium oxide (V₂O_x),^{25,26} and tungsten oxide (WO_x)^{25,27} are often used due to their high work functions. Meanwhile, titanium oxide (TiO_x)^{10,28} and tantalum oxide (Ta₂O_x)^{29,30} have been integrated into Si solar cells as electron-selective contacts due to their suitable electronic properties for band alignment.^{14,31} It is noteworthy that many of the high-efficiency TMO-based solar cells utilize MoO_x and TiO_x films as hole- and electron-selective contacts, respectively.^{10,11,28,32,33} Although a few studies presented the

temperature dependence of V_{oc} and fill factor (FF) of MoO_x-based solar cells,^{34,35} the TC _{η} of these cells has not been reported. For TiO_x-based solar cells, to our knowledge, neither the temperature dependence of cell parameters nor the TCs of these cells has been reported.

In this study, we investigate the temperature-dependent performance of MoO_x- and TiO_x-based solar cells and compare them to that of SHJ cells. We also examine the temperature-dependent behaviour of the surface saturation current density (J_{os}) and the contact resistivity (ρ_c) of those contacts to gain a deeper understanding regarding their impact on TC _{V_{oc}} and the TC of the FF (TC_{FF}), respectively.

2 | EXPERIMENTAL DETAILS

2.1 | Sample preparation

Textured float zone (FZ) n-type wafers (resistivity: 1.7–2.3 Ω·cm, thickness: 190 ± 10 μm) were used to fabricate the solar cells. All the wafers were first cleaned using the Radio Corporation of America (RCA) procedures³⁶ followed by immersion in 5% diluted hydrofluoric (HF) acid. The wafers were then divided into three groups:

1. For the SHJ cells (control cells), a stack of 6-nm hydrogenated intrinsic and 7.5-nm hydrogenated p-doped amorphous Si [a-Si:H(i) and a-Si:H(p), respectively] layers was deposited on the front side using a plasma-enhanced chemical vapour deposition system. A stack of 6-nm a-Si:H(i) and 9.5-nm hydrogenated n-doped amorphous Si [a-Si:H(n)] films was formed on the rear side using the same system.
2. For the MoO_x-based cells, a 6-nm a-Si:H(i) layer was deposited on the front, followed by a 4-nm thermally evaporated MoO_x film. Their rear structure is identical to that of the SHJ cells.
3. For the TiO_x-based cells, the rear side composes a stack of 6-nm a-Si:H(i) film and 1.5-nm TiO_x layer formed by atomic layer deposition (done at 230°C) while their front structure is identical to that of the SHJ cells.

Additional information regarding the conditions used during the depositions can be found in Dréon et al.¹¹ The metallization process of the front contact was similar for the three cell structures; 70-nm indium tin oxide (ITO) film was deposited by a sputtering system through a mask to form active areas of 2 × 2 cm². A silver (Ag) grid was then screen-printed on top of the front ITO film, followed by a curing process at 210°C for the SHJ cells, 130°C for the MoO_x-base cells and 160°C for the TiO_x-based cells for 30 min in air ambient. The rear contacts of the SHJ and MoO_x-based cells were formed by 150-nm sputtered ITO and 100-nm sputtered Ag layers, whereas that of the TiO_x-based cells composes 1-nm thermally evaporated lithium fluoride (LiF) and 200-nm aluminium (Al) films. The LiF film enables an ohmic contact between the TiO_x layer and the Al electrode. Sketches of the investigated devices are shown in Figure 1A–C.

To investigate the temperature-dependent behaviour of the MoO_x- and TiO_x-based passivating contacts, symmetrical lifetime

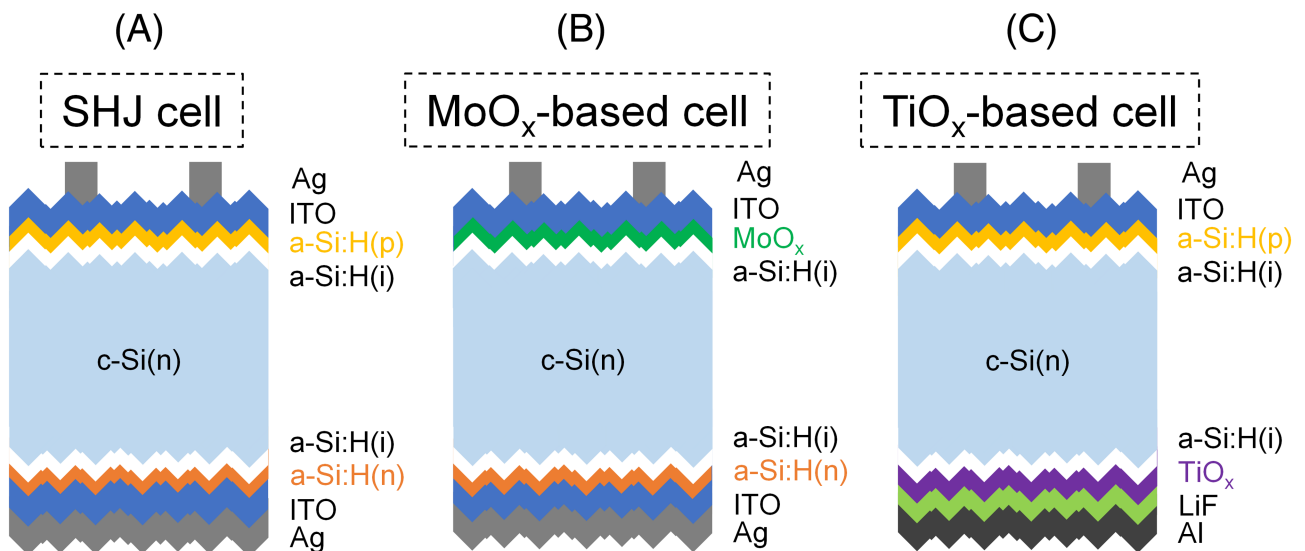


FIGURE 1 Sketches of (A) standard SHJ, (B) MoO_x-based, and (C) TiO_x-based solar cells used in this study

structures for effective lifetime (τ_{eff}) measurements and J_{0s} extraction were prepared using the same wafers, cleaning and deposition processes as the solar cells. The lifetime test wafers were passivated with either a-Si:H(i)/MoO_x or a-Si:H(i)/TiO_x stack on both sides.

To extract ρ_c , Cox and Strack³⁷ test structures were fabricated using both n-type and p-type FZ textured wafers ($1.7\text{--}2.3 \Omega\text{cm}$, $190 \pm 10 \mu\text{m}$). We use p-type wafers for measurements of the MoO_x-based structures to avoid back-to-back diodes. The same layer stacks as for the lifetime test structures were applied to the front side of the Cox and Strack structures, followed by the formation of circular ITO/Ag and LiF/Al contacts with different diameters (from 0.02 to 0.8 cm) on top of the MoO_x and TiO_x layer, respectively. Sputtered Ag (MoO_x-based structures) and thermally evaporated Al (TiO_x-based structures) contacts were applied to the rear side.

The symmetrical lifetime and the Cox and Strack test structures were annealed at 130°C (for the MoO_x-based contacts) and 160°C (for the TiO_x-based contacts) for 30 min in air ambient to mimic the thermal budget of the Ag paste curing process.

A similar set (symmetrical lifetime and Cox and Strack test structures) was also prepared for the a-Si:H(i/p)- and a-Si:H(i/n)-based passivating contacts as references. Sputtered Ag contacts were applied to the rear side of the Cox and Strack structures. The test structures were annealed at 210°C for 30 min in air ambient.

2.2 | Characterization

The current–voltage (I–V) parameters of the solar cells are measured from 25°C to 70°C while Suns- V_{oc} measurements are performed by a customized Sinton Suns- V_{oc} system³⁸ from 80°C to 30°C . The cell's series resistance (R_s) is calculated by comparing the one-sun current density–voltage (J–V) curve to the R_s -free J–V curve obtained from the Suns- V_{oc} measurements.³⁹ TCs are extracted from the slopes of

linear fits of the cell parameters as a function of temperature and are normalized to their values at 25°C (relative TCs).

The external quantum efficiency (EQE) of the studied solar cells is measured by a solar cell spectral response system (QEX7, PV Measurements Inc.).

To extract ρ_c of the passivating contacts, dark I–V measurements are performed on the Cox and Strack structures in the temperature range from 25°C to 80°C .³⁷ The I–V curves of all the test structures have been found to be linear in the voltage range from -0.1 V to $+0.1 \text{ V}$, and the total resistances (R_{tot}) are obtained from the slopes of the linear fits within this range. Note that the rear ohmic contact of these test structures is assumed to have a negligible contribution to the total resistance (R_{tot}). Hence, the obtained ρ_c represents its upper limit.

Sinton lifetime tester (WCT-120TS) is used to measure τ_{eff} as a function of temperature (25°C to 80°C).⁴⁰ J_{0s} is extracted from the τ_{eff} curves using the curve fitting features of Quokka 2⁴¹ and the approach of Dumbrell et al.⁴² The uncertainty in the extracted J_{0s} is calculated from the uncertainty of photoconductance measurements using the approach of McIntosh et al.⁴³ The models of Schenk,⁴⁴ Richter et al.⁴⁵ and Klaassen⁴⁶ are used to determine the effective intrinsic carrier concentration ($n_{i,\text{eff}}$), the intrinsic lifetime and the mobility, respectively.

3 | RESULTS AND DISCUSSION

3.1 | Temperature-dependent performance of solar cells

The cell parameters of the standard SHJ, MoO_x-, and TiO_x-based solar cells as a function of temperature are presented in Figure 2A–D. As expected, for all the investigated solar cells, the V_{oc} , FF, pseudo fill

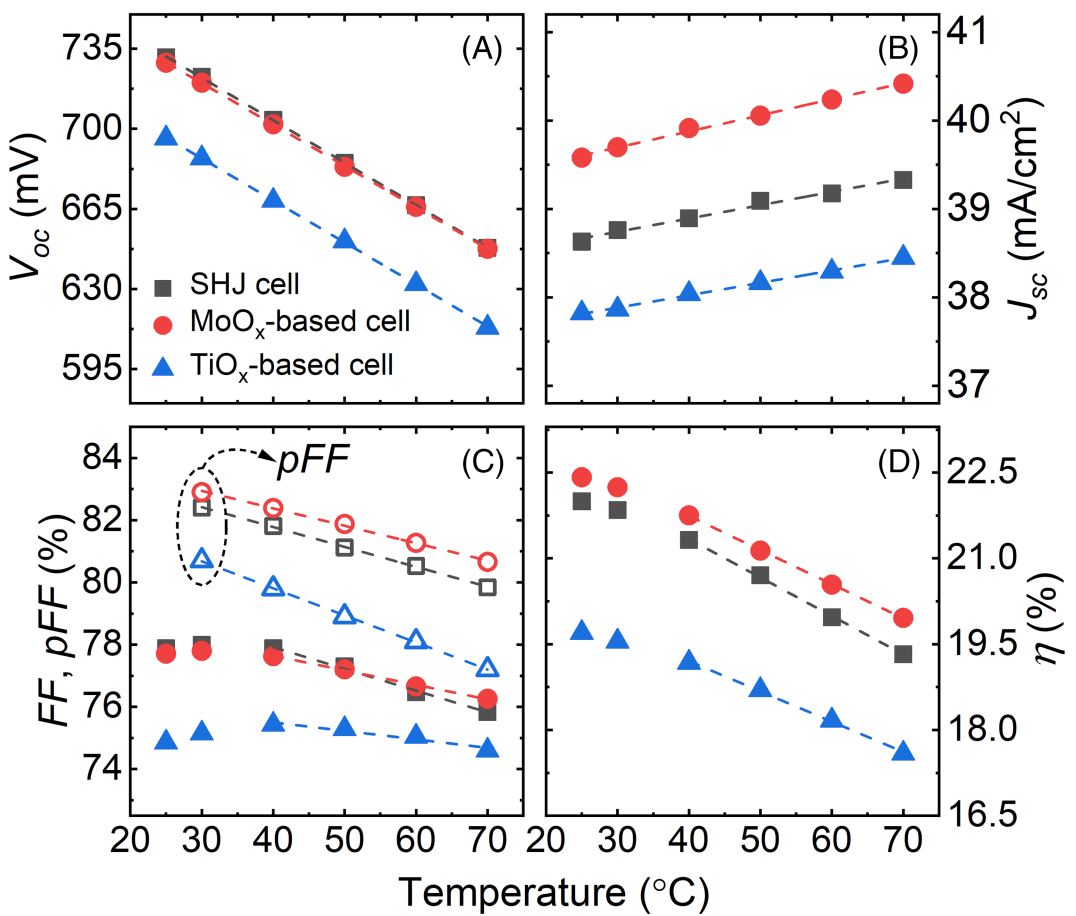


FIGURE 2 Cell parameters of the standard SHJ, MoO_x-, and TiO_x-based solar cells including (A) V_{oc} , (B) J_{sc} , (C) FF and pFF (open symbols), and (D) η under one-sun illumination as a function of temperature

factor (pFF), and efficiency (η) decrease, whereas the short-circuit current density (J_{sc}) increases at elevated temperatures.⁵ The reduction of V_{oc} , FF, and pFF is explained by the increase of n_{eff} at elevated temperatures caused by bandgap narrowing.⁴⁷ The same effect can also explain the improvement of J_{sc} .⁵

Compared to the performance of state-of-the-art devices using MoO_x-based passivating contacts at STC,¹¹ our MoO_x-based cell shows comparable V_{oc} and J_{sc} . Although our FF is lower than that of the champion cell reported in Dréon et al.,¹¹ it is comparable to the average FF stated in the same reference. For the TiO_x-based cell, our cell parameters are slightly lower (by 1.0%_{abs} in efficiency) than those of the state-of-the-art devices reported in Bullock et al.³⁰

The V_{oc} of the MoO_x-based cell is comparable to that of the standard SHJ cell at any given temperature. It seems that the surface passivation in these cells is dominated by the integrated a-Si:H(i) layers.⁴⁸ Meanwhile, the lower V_{oc} of the TiO_x-based cell can be explained by a slight degradation of the rear surface passivation either before the TiO_x deposition (since the deposition was done in a different facility after a long transportation time of a few weeks) or during the TiO_x deposition that was done at 230°C.

It is noteworthy that at any given temperature, the J_{sc} of the MoO_x-based cell is higher than that of the standard SHJ cell. This is

due to the higher optical bandgap of the MoO_x layer compared to that of a-Si:H(p) film,^{34,49–52} resulting in a better spectral response at the short wavelength region (see Figure S1). Meanwhile, the J_{sc} of the TiO_x-based cell is lower than that of the standard SHJ cell despite their identical structure at the front side. This can be attributed to (i) the lower reflectivity of Al compared to that of Ag⁵³ and (ii) the absence of the rear ITO layer. Without the ITO layer, the parasitic absorption within the rear metal layer can be increased.^{54–56} They both result in a low spectral response at the long wavelength region (see Figures 9 and S1).

Compared to the FF of the SHJ solar cell at 25°C, the TiO_x-based cell's FF is lower. It can be explained by the lower V_{oc} of the TiO_x-based cell caused by the slight degradation of the rear surface passivation as mentioned above and the high ρ_c of the TiO_x-based passivating contact (see Figure 7). Non-linear behaviour of the temperature-dependent FF in the temperature range from 25°C to 40°C is observed for all the investigated solar cells. The occurrence of this phenomenon has been reported for standard SHJ^{2,57–59} and MoO_x-based passivating contact solar cells³⁵; however, it has not been reported for TiO_x-based passivating contact solar cells yet. This trend is often attributed to thermionic barriers at the heterojunctions of these cells.^{2,59} The decrease of FF of the MoO_x- and TiO_x-based solar

cells in the temperature range from 40°C to 70°C is less pronounced compared to that of the SHJ solar cell. Note that for all the cells, the decreasing trend of the FF is different from that of the pFF as a function of temperature. This difference can be used to assess the contribution of R_s to the temperature-dependent behaviour of FF, as will be discussed in Section 3.3.

The extracted TCs are summarized in Table 1. The TC_{FF} and TC_η of all the investigated cells are extracted from linear fits in the temperature range from 40°C to 70°C. Using this temperature range minimizes the non-linear effects at low temperatures while still providing information regarding the expected temperature range in the field.¹ The FF and η at 25°C are then obtained by extrapolation to determine

relative TCs. The TCs obtained in this study are compared to those of other cell structures reported in Haschke et al. and Le et al.^{2,22} and presented in Figure 3A–D.

Focusing on TC_{Voc} , it is well known that the temperature sensitivity of V_{oc} of a Si solar cell is defined by the following equation:⁵

$$TC_{Voc} = \frac{dV_{oc}}{dT} = -\frac{E_{g0}/q - V_{oc} + \gamma k_B T/q}{T} \quad (1)$$

where E_{g0} is the semiconductor bandgap linearly extrapolated to 0 K, V_{oc} is reported at the initial temperature (25°C in this study), q is the elementary charge, k_B is the Boltzmann constant and T is the temperature.

TABLE 1 Extracted TCs and the gamma factor (γ), as well as their statistical errors determined from the standard deviation of the linear regression, for the standard SHJ, MoO_x -based, and TiO_x -based solar cells

	TC_{Voc} (%/°C)	TC_{Jsc} (%/°C)	TC_{FF} (%/°C)	TC_{pFF} (%/°C)	TC_η (%/°C)	γ
SHJ cell	-0.254 ± 0.001	$+0.039 \pm 0.002$	-0.088 ± 0.004	-0.077 ± 0.001	-0.301 ± 0.007	3
MoO_x -based cell	-0.248 ± 0.001	$+0.046 \pm 0.001$	-0.059 ± 0.003	-0.067 ± 0.002	-0.264 ± 0.003	2.4
TiO_x -based cell	-0.264 ± 0.001	$+0.037 \pm 0.001$	-0.036 ± 0.006	-0.107 ± 0.001	-0.265 ± 0.008	1.4

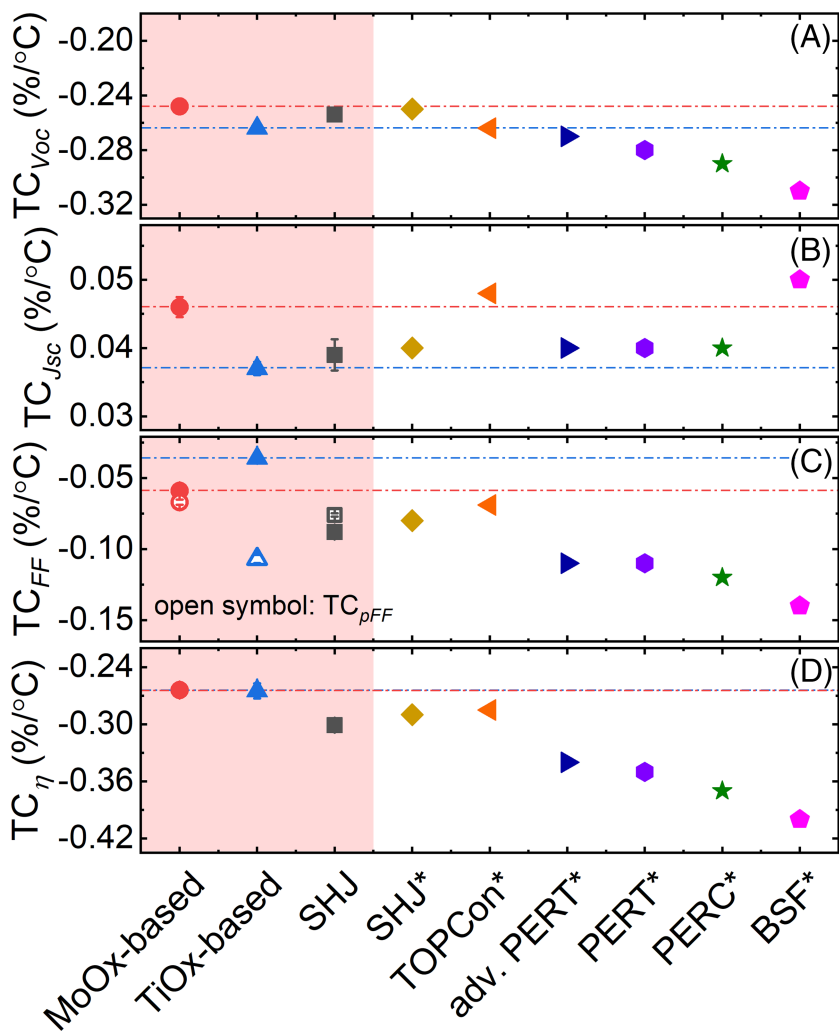


FIGURE 3 (A) TC_{Voc} , (B) TC_{Jsc} , (C) TC_{FF} and TC_{pFF} , and (D) TC_η of the standard SHJ, MoO_x -based, and TiO_x -based solar cells extracted from the slopes of linear fits of the cell parameters as a function of temperature as shown in Figure 2. Error bars are obtained from the linear fits. TCs of solar cell structures reported in the literature^{2,22} (axis labels with star mark) are also shown for comparison

The gamma factor (γ) represents the temperature dependence of the diode saturation current density in the solar cells, and hence, it contains information about the dominant recombination mechanism.^{1,60} The extracted values for γ using Equation 1 are summarized in Table 1. Here, we use E_{g0} of 1.206 eV for all the calculations of the studied cells due to their similar wafer resistivity.⁶¹ The TC_{Voc} of the MoO_x -based cell is slightly superior to that of the standard SHJ cell, despite a negligible difference between the initial V_{oc} of the two cell structures (731.2 mV [standard SHJ] and 728.9 mV [MoO_x -based] at 25°C). The different TC_{Voc} can be explained by different γ (see Table 1), suggesting that V_{oc} of these cells is limited by different mechanisms. The inferior TC_{Voc} of the TiO_x -based cell is expected as its initial V_{oc} is lower than those of the standard SHJ and MoO_x -based cells. For this cell structure, the impact of V_{oc} on TC_{Voc} is being dominant over that of γ .

Compared to the TC_{Voc} of other cell structures as shown in Figure 3A, the obtained TC_{Voc} of the MoO_x -based solar cell is comparable to that of the SHJ cells while the TiO_x -based cell's TC_{Voc} is almost identical to the tunnel oxide passivated contact (TOPCon) cells' TC_{Voc} . The TC_{Voc} of both MoO_x - and TiO_x -based cells is superior to those of the cells without passivating contacts (PERC, PERT, Al back surface field [Al-BSF], etc.). Battaglia et al.³⁴ and Sacchetto et al.³⁵ reported that the decreasing trend of V_{oc} of the MoO_x -based cells is less pronounced compared to that of the SHJ cells as a function of temperature. This implies a superior TC_{Voc} of the MoO_x -based cells, agreeing with our findings.

The TC_{Jsc} of the TiO_x -based solar cell is comparable to that of the standard SHJ cell, whereas the TC_{Jsc} of the MoO_x -based cell is more favourable than those of the former two cells. The spectral response of the studied cells at different temperatures will be presented and discussed in Section 3.5 to clarify this trend. The TC_{Jsc} of the MoO_x -based cell is comparable to that of the TOPCon cell and better than those of all the others, except for the Al-BSF cell (the superior TC_{Jsc} of the Al-BSF cell is discussed in Le et al.²²). Meanwhile, the TC_{Jsc} of the SHJ and TiO_x -based cells is comparable to those of the advanced PERT, PERT, and PERC cells.

The TC_{FF} of the MoO_x - and TiO_x -based solar cells is superior to those of any other cell (in the range above 40°C), including the SHJ. Furthermore, their TC_{FF} is better than their TC_{pFF} , whereas the standard SHJ cell shows an opposite trend. This indicates that R_s of the two former cells reduces at elevated temperatures while the latter cell's R_s increases. The temperature-dependent behaviour of R_s of the investigated cells will be discussed in Section 3.3. To quantify the contribution of V_{oc} and R_s to TC_{FF} of the studied cells, the following equations are used:^{62,63}

$$\frac{1}{FF} \frac{dFF}{dT} = (1 - 1.02FF_0) \left(\frac{1}{V_{oc}} \frac{dV_{oc}}{dT} - \frac{1}{T} \right) - \frac{R_s}{V_{oc}/I_{sc} - R_s} \left(\frac{1}{R_s} \frac{dR_s}{dT} \right) \quad (2)$$

where

$$FF_0 = \frac{\nu_{oc} - \ln(\nu_{oc} + 0.72)}{\nu_{oc} + 1} \quad (3)$$

where FF_0 is the FF in the absence of R_s and shunt resistance (R_{sh}) effects and ν_{oc} is the normalized V_{oc} to the thermal voltage (nkT/q).

The first term in Equation 2 represents the contribution of V_{oc} to TC_{FF} while the second term indicates the contribution of R_s to TC_{FF} . For the cell structures studied here, the contribution of V_{oc} to TC_{FF} is dominant and accounts for more than 60%, indicating that the temperature-dependent behaviour of FF strongly depends on the increase of n_{eff} at elevated temperatures caused by bandgap narrowing.⁴⁷ It is noteworthy that the contribution of R_s to TC_{FF} is considerably more significant for the TiO_x -based cell (nearly 36%) than for the other studied cells. It offsets the decrease of the TiO_x -based cell's V_{oc} at elevated temperature, resulting in a greatly superior TC_{FF} of this cell.

The TC_η of the MoO_x - and TiO_x -based solar cells is almost identical. They are better than that of the standard SHJ cell and greatly superior to those of other cell structures reported in the literature. The obtained TC_η highlights the advantage of using TMO-integrated cells in the field. As expected, the contribution of TC_{Voc} to TC_η is larger than the contributions of TC_{FF} and TC_{Jsc} and accounts for more than 60% for all the cell structures shown in Figure 3. Battaglia et al.³⁴ and Sacchetto et al.³⁵ also reported that the decreasing trend of the MoO_x -based cells' efficiency is less pronounced compared to that of the SHJ cells' efficiency as a function of temperature. This implies a favourable TC_η of the MoO_x -based cells in agreement with our findings.

Since the TC_η of the TiO_x -based cells is superior to that of the SHJ cells, it is expected that the performance difference between the structures will reduce at higher temperatures. As the efficiency of the TiO_x cell is relatively low at 25°C, its better TC_η is not expected to compensate for the entire difference in the typical operating temperature range. Nevertheless, avoiding the slight degradation of the rear surface passivation and maintaining a similar TC_η will ensure comparable efficiencies of the TiO_x -based and the SHJ cells at 70°C.

3.2 | Temperature and illumination intensity dependence of solar cells

In Section 3.1, we discussed the temperature sensitivity of the cell parameters at one-sun. However, in the field, solar cells do not only operate at different temperatures, but they are also exposed to a large range of illumination intensities. Since TC_{Voc} dominates TC_η for all the studied cells, it can indicate the temperature sensitivity of the cells at different intensities. Owing to our customized Suns- V_{oc} tool, measurements can be done in a wide range of illumination intensities (from 0.001 suns to >100 suns), which enable deeper insights into the temperature-dependent performance of Si solar cells for different applications. Although the illumination intensity range from 0.1 sun to 1 sun is the most relevant for terrestrial PV applications, the information at higher illumination intensities can be used for concentrator cells⁶⁴ while the performance at lower intensities may be valuable for the Internet of Things applications.

Suns- V_{oc} measurements of the investigated cells in the temperature range from 30°C to 80°C are presented in Figure 4A-C. For all three cell structures, a significant reduction of V_{oc} with increasing

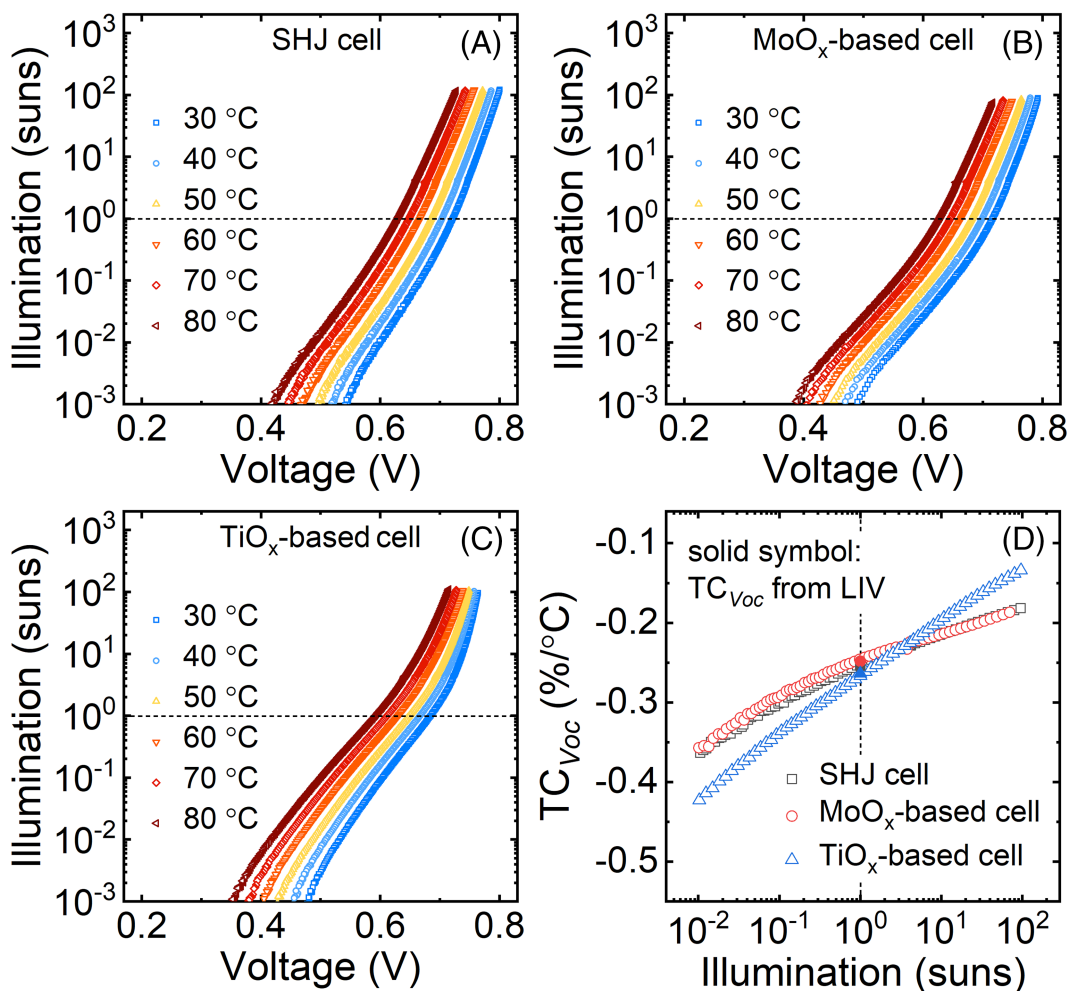


FIGURE 4 Suns- V_{oc} measurements of (A) the standard SHJ, (B) MoO_x-, and (C) TiO_x-based solar cells at different temperatures. (D) TC_{Voc} extracted from Suns- V_{oc} (open symbols) and I-V (solid symbols) measurements as a function of illumination intensity

temperature can be seen at low illumination intensities. This reduction is less pronounced at higher illumination intensities. TC_{Voc} of the studied cells extracted from Suns- V_{oc} measurements (open symbols) as a function of illumination intensity is presented in Figure 4D. TC_{Voc} obtained from I-V measurements (solid symbols) at one sun illumination is also shown for comparison. We find that the TC_{Voc} at one sun illumination extracted from both measurement methods matches well (in the range of 1.2%). For all the cells, the absolute value of TC_{Voc} decreases with increasing illumination intensity (less negative), indicating that the studied cells are less sensitive to temperature variation at higher illumination intensities. It is noteworthy that the TC_{Voc} of the MoO_x-based and SHJ cells behave similarly as a function of illumination intensity while the illumination intensity dependence of TC_{Voc} is more pronounced for the TiO_x-based cell. For most of the intensity range, this observation can be attributed to the lower initial V_{oc} of the TiO_x-based cell compared to the initial V_{oc} of the other cells (see Figure S2). However, at high illumination intensities (>3 suns), it seems that the impact of γ on the TC_{Voc} of the TiO_x-based cell becomes significant.

3.3 | Temperature dependence of R_s

Figure 3C highlights the superiority of TMO-based solar cells regarding TC_{FF}. As mentioned, we expect that R_s of the MoO_x- and TiO_x-based solar cells reduces at elevated temperatures, whereas the standard SHJ cell's R_s increases. This section investigates the temperate dependence of the studied cells' R_s and several components that contribute to R_s to explain the findings.

R_s of the studied cells as a function of temperature is shown in Figure 5. Indeed, R_s of the MoO_x- and TiO_x-based solar cells reduces with increasing temperature while the standard SHJ cell's R_s increases. As expected from the difference between TC_{FF} and TC_{pFF} of these cells (see Figure 3C), the reduction of the TiO_x-based cell's R_s at elevated temperatures is more pronounced compared to that of the MoO_x-based cell's R_s . The extracted TC_{Rs} of the studied solar cells is summarized in Table 2. Note that the R_{sh} of these cells, as determined from the linear fit of the I-V measurement around $V = 0$ V (not shown here), is extremely large (in the range of 10 k-30 k Ω ·cm²). R_{sh} is therefore assumed not to impact the temperature dependence of FF.

R_s of the studied cells consists of the contributions of the rear metal contact, the electron-collector ($R_{e\text{-}col(r)}$), the Si wafer, the hole-collector ($R_{h\text{-}col(f)}$), the lateral transport within the front ITO layer, the interfacial contact between the front ITO layer and the front metal contacts and the front metal contacts including fingers and busbars. $R_{e\text{-}col(r)}$ and $R_{h\text{-}col(f)}$ can be obtained from the ρ_c test structures. Since the temperature of the curing process after metallization is different for the investigated solar cells (see Section 2.1), the possibility that this process varies the contribution of the other components to the

cells' R_s might not be excluded. Note that $R_{e\text{-}col(r)}$ and $R_{h\text{-}col(f)}$ obtained from the ρ_c test structures represent their upper limit. They will be presented in the next sections.

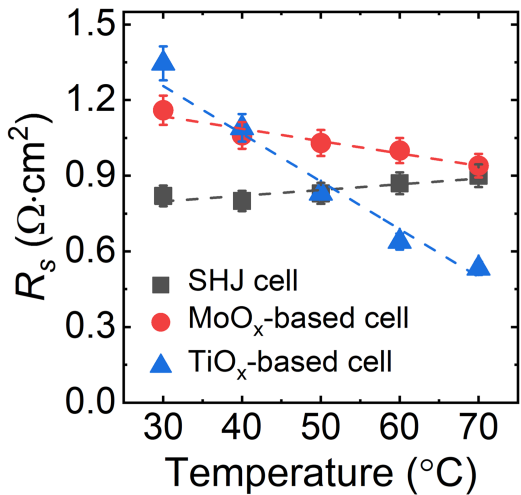


FIGURE 5 R_s of the standard SHJ, MoO_x -, and TiO_x -based solar cells as a function of temperature

3.3.1 | Temperature dependence of the contact resistivity of the hole-collector

To gain a deeper understanding regarding the difference between the standard SHJ and MoO_x -based cells, the a-Si:H(i/p)- and MoO_x -based test structures are studied. Figure 6 presents ρ_c obtained from these structures as a function of temperature. Interestingly, the temperature dependence of ρ_c shows opposite trends. When the temperature increases from 25°C to 80°C, the ρ_c of the a-Si:H(i/p)-based structures increases from 0.17 to 0.23 $\Omega \cdot \text{cm}^2$, whereas the ρ_c of the MoO_x -based structures decreases from 0.32 to 0.17 $\Omega \cdot \text{cm}^2$. The carrier transport via thermionic barrier is usually improved at elevated temperatures.⁵⁸ Therefore, the significant decrease of ρ_c of the MoO_x -based structures may indicate a large thermionic component in the carrier transport across the contact. Meanwhile, the ρ_c increase of the a-Si:H(i/p)-based structures may imply that the carrier transport via thermionic barrier in this contact becomes less pronounced. It is noteworthy that the rate of change of the ρ_c against temperature for the two test structures is lower than that of the R_s for the corresponding cells, indicating that other components also contribute to the temperature-dependent behaviour of their R_s . It seems that the improvement of ρ_c of the MoO_x -based structures at elevated temperatures counterbalances some of the FF losses, resulting in a less temperature-sensitive FF.

TABLE 2 Extracted TC_{Rs} and their statistical errors of the linear regression determined from the standard deviation for the standard SHJ, MoO_x -, and TiO_x -based solar cells

	Standard SHJ cell	MoO_x -based cell	TiO_x -based cell
TC _{Rs} (%/°C)	+0.281 ± 0.082	-0.414 ± 0.057	-1.314 ± 0.149

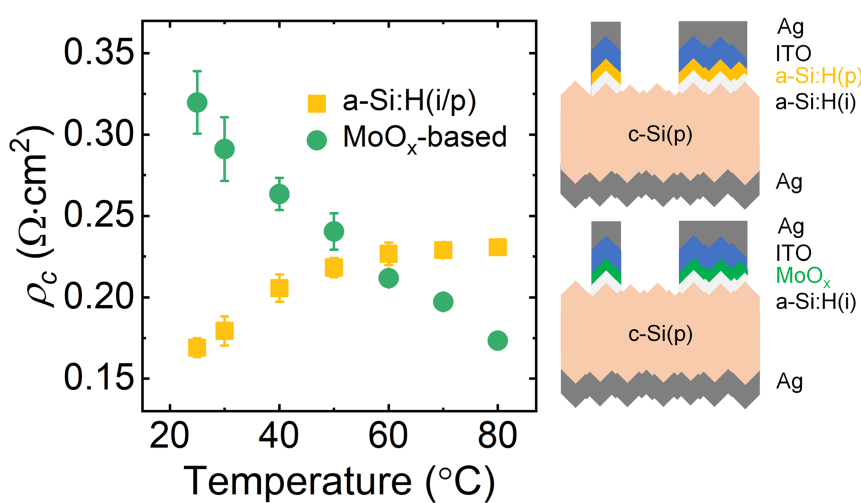


FIGURE 6 ρ_c of the a-Si:H(i/p)- and MoO_x -based test structures as a function of temperature. Sketches of the Cox and Strack test structures are shown next to the figure

FIGURE 7 ρ_c of the a-Si:H(i/n)- and TiO_x -based test structures as a function of temperature. Sketches of the Cox and Strack test structures are shown next to the figure. The inset compares ρ_c of the a-Si:H(i/p)- (open symbols) and a-Si:H(i/n)-based (solid symbols) test structures

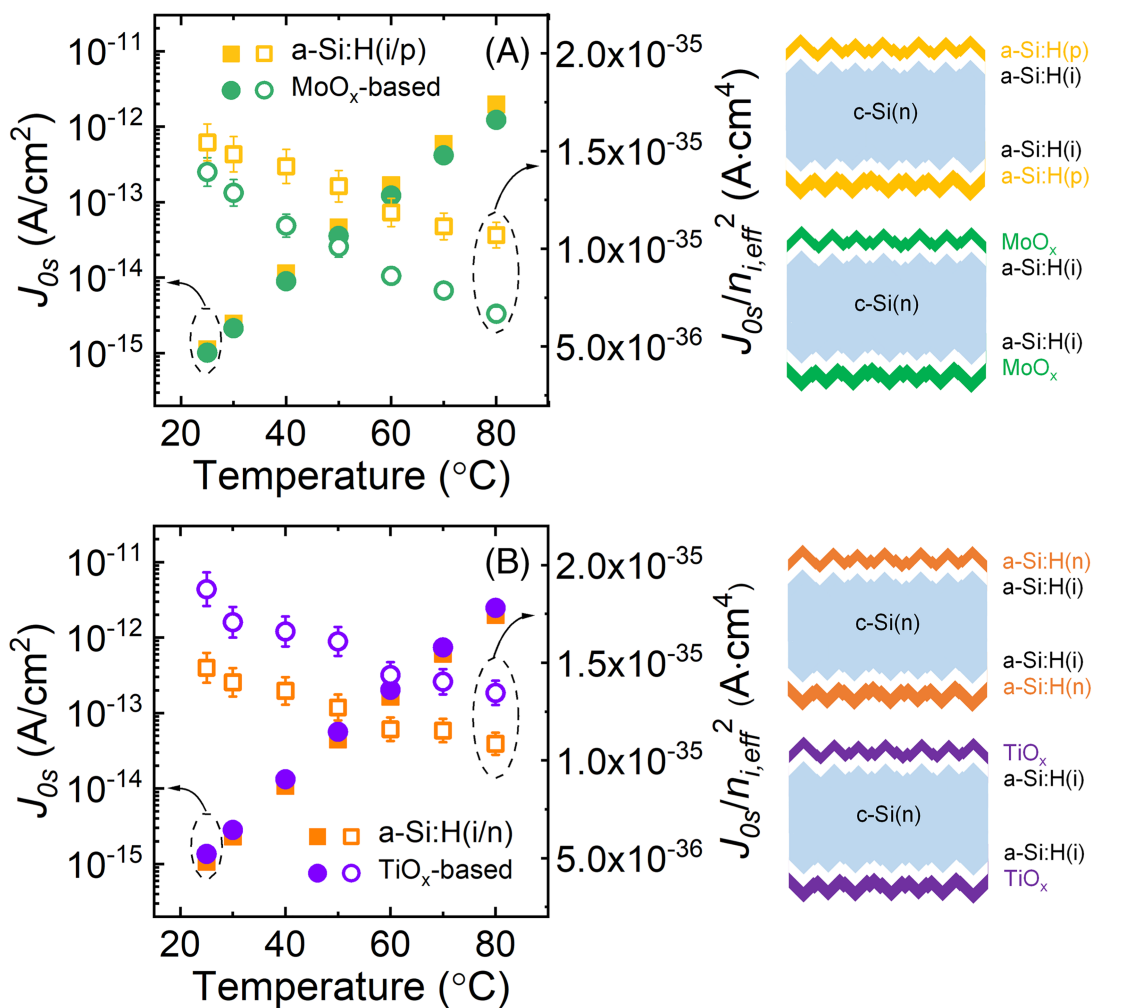
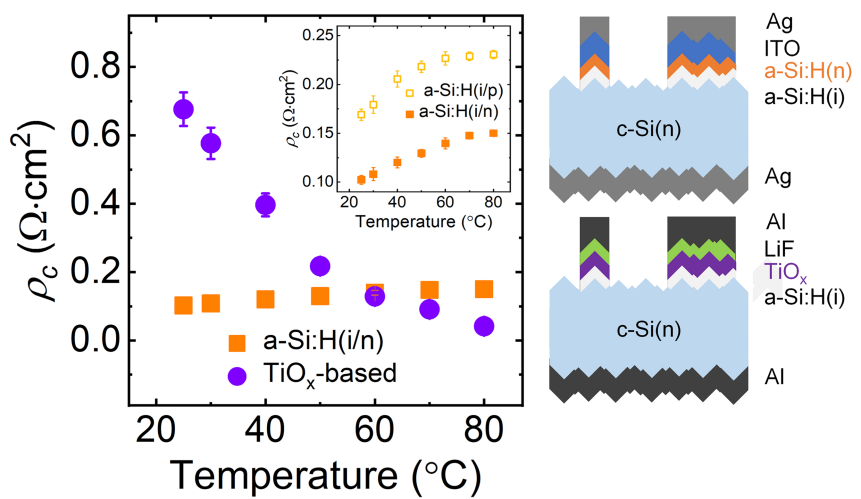


FIGURE 8 J_{0s} and $J_{0s}/n_i,eff^2$ ratios of (A) the a-Si:H(i/p)- and MoO_x -based and (B) the a-Si:H(i/n)- and TiO_x -based lifetime test structures as a function of temperature. Sketches of the symmetrical lifetime test structures used in this study are shown next to the figures

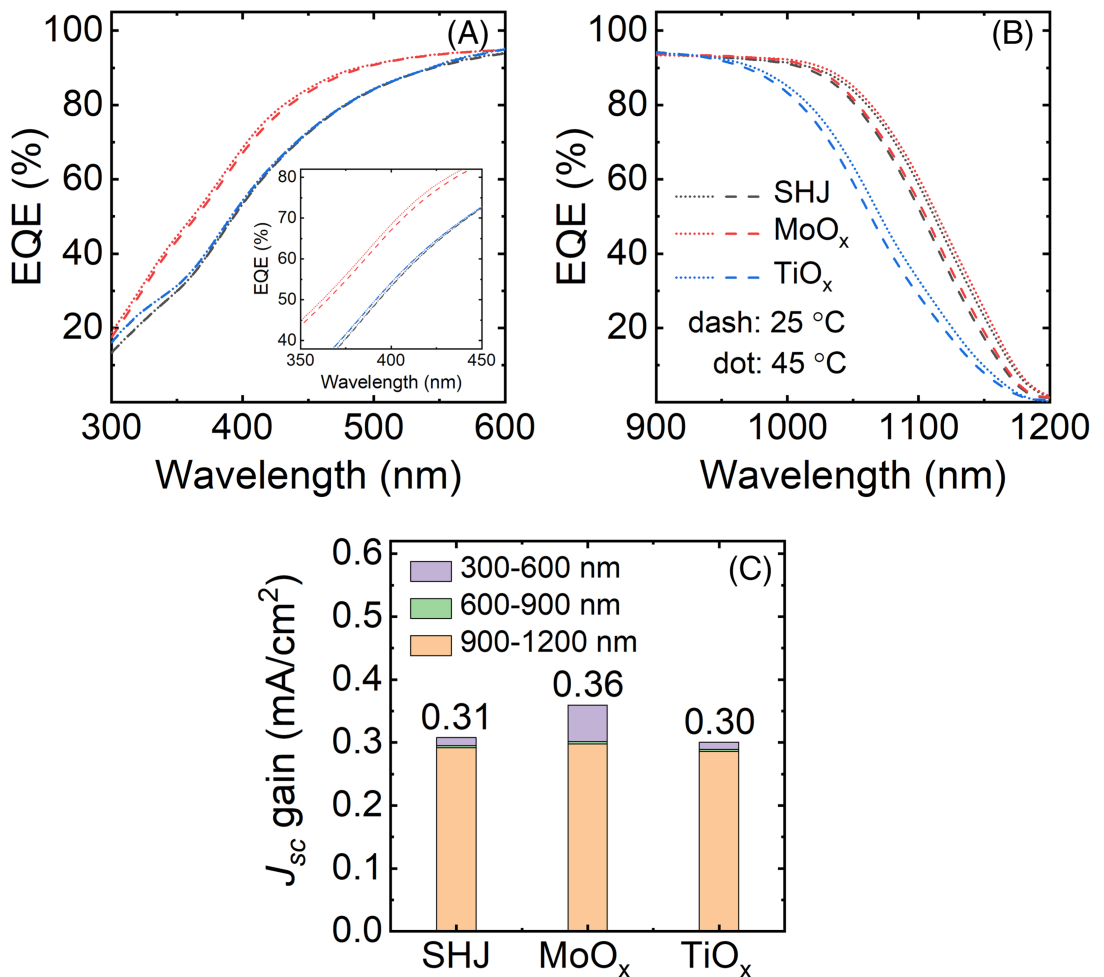


FIGURE 9 EQE measurements of the standard SHJ, MoO_x-based, and TiO_x-based solar cells at 25°C and 45°C in the range of wavelength (A) from 300 to 600 nm and (B) from 900 to 1200 nm. (C) J_{sc} gain between 25°C and 45°C at different wavelength regions

	a-Si:H(i/p)	MoO _x -based	a-Si:H(i/n)	TiO _x -based
$TC_{J_{0s}/n_{i,eff}^2} (\%/\text{°C})$	-0.56 ± 0.02	-0.90 ± 0.03	-0.46 ± 0.05	-0.47 ± 0.05

TABLE 3 Extracted TCs of the $J_{0s}/n_{i,eff}^2$ ratio and their statistical errors determined from the standard deviation of the linear regression for the a-Si:H- and TMO-based lifetime test structures

3.3.2 | Temperature dependence of the contact resistivity of the electron-collector

To compare between the standard SHJ and TiO_x-based cells, the a-Si:H(i/n)- and TiO_x-based test structures are investigated. Figure 7 presents ρ_c obtained from these structures as a function of temperature. The extracted ρ_c at STC of both structures is comparable to those previously reported.^{52,58} Again, an opposite trend is observed. When the temperature increases from 25°C to 80°C, the ρ_c of the a-Si:H(i/n)-based structures increases from 0.10 to 0.15 Ω·cm², whereas the ρ_c of the TiO_x-based structures decreases from 0.68 to 0.04 Ω·cm². As in the previous section, a large thermionic component in the carrier transport can explain the significant decrease of ρ_c of the TiO_x-based structures.⁵⁸ We also find that the rate of change of the ρ_c against

temperature for the two test structures is lower than that of the two corresponding cells' R_s . Similar to the MoO_x-based structures, the improvement of ρ_c of the TiO_x-based structures with increasing temperature counterbalances some of the FF losses of this cell, resulting in its favourable TC_{FF} .

As shown in Figures 6 and 7, the a-Si:H-based test structures' ρ_c increases at elevated temperatures, and its rate of change against temperature is lower than that of the TMO-based structures' ρ_c , indicating less temperature sensitivity of the former structures. This is probably due to the efficient temperature-independent tunneling transport in the a-Si:H-based passivating contacts.⁵⁸ Compared to the a-Si:H(i/p)-based test structures, the ρ_c of the a-Si:H(i/n)-based test structures is lower at any given temperature as shown in the inset of Figure 7. This phenomenon was also reported in Nogay et al.⁵⁸ and

can be explained by the usually much smaller conduction band offset in the a-Si:H(i/n)-based structure compared to the valence band offset in the a-Si:H(i/p)-based structures.⁶⁵ Thus, the hole transport is impeded by the a-Si:H(i) layer.⁶⁵

3.4 | Temperature dependence of surface passivation

In this section, we investigate the temperature-dependent behaviour of J_{0s} , one of the key parameters indicating the quality of a passivating contact. The extracted J_{0s} values using lifetime measurements on the symmetrical test structures as a function of temperature are depicted Figure 8A,B. We observe a significant increase of J_{0s} , which is due to the increase of $n_{i,\text{eff}}$ caused by bandgap narrowing,⁴⁷ since J_{0s} is proportional to $n_{i,\text{eff}}^2$.⁶⁶ More meaningful information is obtained from the $J_{0s}/n_{i,\text{eff}}^2$ ratio as a function of temperature. If the rise in J_{0s} at elevated temperatures is solely determined by $n_{i,\text{eff}}$, the ratio needs to be temperature independent. As a reduction of the ratios with increasing temperature is observed regardless of the test structures, an improvement of the passivation quality at elevated temperature can be assumed. TCs of the $J_{0s}/n_{i,\text{eff}}^2$ ratio are extracted and summarized in Table 3. The improvement is more pronounced for the MoO_x-based lifetime test structures compared to the other structures. Nevertheless, it seems that the improvement of the passivation quality observed for all the lifetime test structures does not have a strong impact on TC_{Voc} of the investigated solar cells. Note that in the real devices, the possibility that the metal contact impacts both the passivation quality and its temperature dependence might not be excluded.

3.5 | Temperature dependence of EQE

As discussed above, the TC_{Jsc} of the TiO_x-based solar cell is comparable to that of the standard SHJ cell, whereas the TC_{Jsc} of the MoO_x-based cell is superior to those of the former two cell structures. Furthermore, in the previous section, we noticed that the passivation quality obtained by MoO_x shows stronger improvement with temperature compared to the other passivation schemes. In this section, we use temperature-dependent EQE measurements to shine more light on these findings.

The EQE measurements of the studied solar cells at 25°C and 45°C in the wavelength ranges of 300–600 nm (short wavelengths) and 900–1200 nm (long wavelengths) are presented in Figure 9A,B, respectively. For the short wavelength region, the EQE at the two temperatures is almost identical for the standard SHJ and TiO_x-based cells, whereas a slight increase is observed for the MoO_x-based cell. For the long wavelength region, the spectral response is improved with increasing temperature, regardless of the cell structures. This improvement is attributed to bandgap narrowing of the Si at elevated temperatures^{1,38} that has a critical impact on this wavelength range.

The gain of J_{sc} between 25°C and 45°C determined from the EQE, split into different wavelength ranges, is presented in Figure 9C.

The J_{sc} of the MoO_x-based cell gains 0.36 mA/cm², 0.05–0.06 mA/cm² higher than the J_{sc} gain of the other two cells. The J_{sc} gains in the wavelength ranges of 600–900 and 900–1200 nm are almost identical for all the cells, whereas the J_{sc} gain in the wavelength range of 300–600 nm is different.

Since the optical properties of MoO_x films are almost identical at 25°C and 45°C (see Figure S3), the better spectral response at short wavelengths of the MoO_x-based cell can therefore be explained by the larger improvement of the passivation quality with increasing temperature of this structure (Section 3.4). To strengthen this point, we established a model using the AFORS-HET simulation tool⁶⁷ and successfully reproduce the trend of the spectral response at the short wavelength region by modifying the ratio between the electron and hole capture cross sections (σ_n/σ_p). Hence, the favourable TC_{Jsc} of the MoO_x-based cell can be attributed to the large improvement of the passivation quality of the MoO_x-based passivating contacts, resulting in the increase of the spectral response at elevated temperatures in the short wavelength range.

4 | CONCLUSION

The temperature-dependent performance of TMO-based passivating contacts and their devices was investigated. The TC_{η} of the MoO_x- and TiO_x-based solar cells is almost identical. They are better than that of the standard SHJ cell and greatly superior to those of the cell structures without passivating contacts. In terms of the temperature sensitivity, the findings highlight the advantage of using solar cells that integrate TMO-based passivating contacts in the field. Moreover, knowledge of their TC_{η} and insights into their performance at various operating temperatures enable an accurate estimate of the annual energy yield of PV systems using TMO-based technology and hence a comparison to other technologies.

The superior TC_{η} of the MoO_x-based cell is mainly due to the favourable TC_{Jsc} and TC_{FF} while the TC_{η} superiority of the TiO_x-based cell is solely from a superior TC_{FF} . The favourable TC_{Jsc} of the MoO_x-based cell compared to the other two cell structures can be explained by a better spectral response at the short wavelength region with increasing temperature, resulting from an improvement in the passivation quality of the MoO_x-based passivating contacts. The superior TC_{FF} of the MoO_x- and TiO_x-based solar cells is partly contributed by the improvement of ρ_c of their passivating contacts at elevated temperatures which counterbalances some of the FF losses, resulting in a less temperature-sensitive FF.

Furthermore, it was concluded that the studied cells are less sensitive to temperature variation at higher illumination intensities. The TC_{Voc} of the MoO_x-based and SHJ cells behave the same as a function of illumination intensity while the illumination intensity dependence is more pronounced for the TiO_x-based cell.

ACKNOWLEDGEMENTS

The authors thank Simon M. F. Zhang for his help with the transmission measurements. This work was funded by the Australian

Government through Australian Renewable Energy Agency (ARENA; project 2017/RND001). The views expressed herein are not necessarily the views of the Australian Government, and the Australian Government does not accept responsibility for any information or advice contained herein. This work was also supported by the Swiss National Science Foundation under Ambizione Energy grant ICONS (PZENP2_173627).

CONFLICT OF INTEREST

The authors declare that they have no conflicts of interest.

DATA AVAILABILITY STATEMENT

Data sharing is not applicable to this article as no datasets were generated or analysed during the current study.

ORCID

Anh Huy Tuan Le  <https://orcid.org/0000-0002-9395-0771>

REFERENCES

- Dupré O, Vaillon R, Green MA. *Thermal Behavior of Photovoltaic Devices*. Vol. 10. Springer; 2017.
- Haschke J, Seif JP, Riesen Y, et al. The impact of silicon solar cell architecture and cell interconnection on energy yield in hot & sunny climates. *Energy Environ Sci*. 2017;10(5):1196-1206.
- Kasu M, Abdu J, Hara S, Choi S, Chiba Y, Masuda A. Temperature dependence measurements and performance analyses of high-efficiency interdigitated back-contact, passivated emitter and rear cell, and silicon heterojunction photovoltaic modules. *Jpn J Appl Phys*. 2018;57(8S3):08RG18-1-08RG18-7.
- Singh P, Ravindra NM. Temperature dependence of solar cell performance—an analysis. *Sol Energ Mat Sol C*. 2012;101:36-45.
- Green MA. General temperature dependence of solar cell performance and implications for device modelling. *Prog Photovolt Res Appl*. 2003;11(5):333-340.
- Haase F, Hollemann C, Schafer S, et al. Laser contact openings for local poly-Si-metal contacts enabling 26.1%-efficient POLO-IBC solar cells. *Sol Energ Mat Sol C*. 2018;186:184-193.
- Nandakumar N, Rodriguez J, Kluge T, et al. Approaching 23% with large-area monoPoly cells using screen-printed and fired rear passivating contacts fabricated by inline PECVD. *Prog Photovolt Res Appl*. 2019;27(2):107-112.
- Yoshikawa K, Kawasaki H, Yoshida W, et al. Silicon heterojunction solar cell with interdigitated back contacts for a photoconversion efficiency over 26%. *Nat Energy*. 2017;2(5):17032-1-17032-8.
- Richter A, Benick J, Feldmann F, Fell A, Hermle M, Glunz SW. n-type Si solar cells with passivating electron contact: Identifying sources for efficiency limitations by wafer thickness and resistivity variation. *Sol Energ Mat Sol C*. 2017;173:96-105.
- Bullock J, Wan Y, Hettick M, et al. Dopant-free partial rear contacts enabling 23% silicon solar cells. *Adv Energy Mater*. 2019;9(9):1803367-1-1803367-6.
- Dréon J, Jeangros Q, Cattin J, et al. 23.5%-efficient silicon heterojunction silicon solar cell using molybdenum oxide as hole-selective contact. *Nano Energy*. 2020;70:104495-1-104495-7.
- Yang X, Liu W, de Bastiani M, et al. Dual-function electron-conductive, hole-blocking titanium nitride contacts for efficient silicon solar cells. *Joule*. 2019;3(5):1314-1327.
- Cuevas A, Wan YM, Yan D, et al. Carrier population control and surface passivation in solar cells. *Sol Energ Mat Sol C*. 2018;184:38-47.
- Allen TG, Bullock J, Yang X, Javey A, de Wolf S. Passivating contacts for crystalline silicon solar cells. *Nat Energy*. 2019;4(11):1-15.
- Melskens J, van de Loo BWH, Macco B, Black LE, Smit S, Kessels WMM. Passivating contacts for crystalline silicon solar cells: From concepts and materials to prospects. *IEEE J Photovolt*. 2018;8(2):373-388.
- Yang X, Weber K, Hameiri Z, de Wolf S. Industrially feasible, dopant-free, carrier-selective contacts for high-efficiency silicon solar cells. *Prog Photovolt Res Appl*. 2017;25(11):896-904.
- Zhong S, Morales-Masis M, Mews M, et al. Exploring co-sputtering of ZnO:Al and SiO₂ for efficient electron-selective contacts on silicon solar cells. *Sol Energ Mat Sol C*. 2019;194:67-73.
- Adachi D, Hernández JL, Yamamoto K. Impact of carrier recombination on fill factor for large area heterojunction crystalline silicon solar cell with 25.1% efficiency. *Appl Phys Lett*. 2015;107(23):233506-1-233506-3.
- Masuko K, Shigematsu M, Hashiguchi T, et al. Achievement of more than 25% conversion efficiency with crystalline silicon heterojunction solar cell. *IEEE J Photovolt*. 2014;4(6):1433-1435.
- Yoshikawa K, Kawasaki H, Yoshida W, et al. Silicon heterojunction solar cell with interdigitated back contacts for a photoconversion efficiency over 26%. *Nat Energy*. 2017;2(5):1-8.
- Haase F, Hollemann C, Schäfer S, et al. Laser contact openings for local poly-Si-metal contacts enabling 26.1%-efficient POLO-IBC solar cells. *Sol Energ Mat Sol C*. 2018;186:184-193.
- Le AHT, Basnet R, Yan D, et al. Temperature-dependent performance of silicon solar cells with polysilicon passivating contacts. *Sol Energ Mat Sol C*. 2021;225:111020-1-111020-7.
- Le AHT, Basnet R, Yan D, Chen W, Seif JP, Hameiri Z. Temperature dependence of polysilicon passivating contact and its device performance. *47th IEEE Photovoltaic Specialists Conference*. 2020; 1020-1023.
- Bullock J, Yan D, Cuevas A, Wan Y, Samundsett C. n-and p-typesilicon solar cells with molybdenum oxide hole contacts. *Energy Procedia*. 2015;77:446-450.
- Gerling LG, Mahato S, Morales-Vilches A, et al. Transition metal oxides as hole-selective contacts in silicon heterojunctions solar cells. *Sol Energ Mat Sol C*. 2016;145:109-115.
- Yang X, Xu H, Liu W, et al. Atomic layer deposition of vanadium oxide as hole-selective contact for crystalline silicon solar cells. *Advanced Electronic Materials*. 2020;6(8):2000467-1-2000467-8.
- Essig S, Dréon J, Werner J, et al. MoO_x and WO_x based hole-selective contacts for wafer-based Si solar cells. 2017 IEEE 44th Photovoltaic Specialist Conference (PVSC) 2017.
- Wang W, He J, Yan D, et al. 21.3%-efficient n-type silicon solar cell with a full area rear TiO_x/LiF/Al electron-selective contact. *Sol Energ Mat Sol C*. 2020;206:110291-1-110291-4.
- Wan YM, Samundsett C, Bullock J, et al. Conductive and stable magnesium oxide electron-selective contacts for efficient silicon solar cells. *Adv Energy Mater*. 2017;7(5):1601863-1-1601863-7.
- Bullock J, Wan Y, Xu Z, et al. Stable dopant-free asymmetric heterocontact silicon solar cells with efficiencies above 20%. *ACS Energy Letters*. 2018;3(3):508-513.
- Yang X, Lin Y, Liu J, et al. A highly conductive titanium oxynitride electron-selective contact for efficient photovoltaic devices. *Adv Mater*. 2020;32(32):2002608-1-2002608-8.
- Geissbühler J, Werner J, Martin de Nicolas S, et al. 22.5% efficient silicon heterojunction solar cell with molybdenum oxide hole collector. *Appl Phys Lett*. 2015;107(8):081601-1-081601-5.
- Wu W, Lin W, Zhong S, et al. 22% efficient dopant-free interdigitated back contact silicon solar cells. *AIP Conference Proceedings*. 2018; 1999(1):040025-1-040025-6.
- Battaglia C, de Nicolas SM, de Wolf S, et al. Silicon heterojunction solar cell with passivated hole selective MoO_x contact. *Appl Phys Lett*. 2014;104(11):113902-1-113902-5.

35. Sacchetto D, Jeangros Q, Christmann G, et al. ITO/MoO_x/a-Si:H (i) hole-selective contacts for silicon heterojunction solar cells: Degradation mechanisms and cell integration. *IEEE J Photovolt*. 2017;7(6): 1584-1590.
36. Kern W. The evolution of silicon-wafer cleaning technology. *J Electrochim Soc*. 1990;137(6):1887-1892.
37. Cox RH, Strack H. Ohmic contacts for GaAs devices. *Solid State Electron*. 1967;10(12):1213-1218.
38. Zhang SMF, Seif JP, Allen TG, et al. Temperature- and illumination-dependent characterization of solar cells using Suns-V_{OC}(T) and I-V (T). 48th IEEE Photovoltaic Specialists Conference. 2021.
39. Wolf M, Rauschenbach H. Series resistance effects on solar cell measurements. *Advanced Energy Conversion*. 1963;3(2):455-479.
40. Zhu Y, Rougieux F, Grant NE, et al. Electrical characterization of thermally activated defects in n-type float-zone silicon. *IEEE J Photovolt*. 2020;11(1):26-35.
41. Fell A. A free and fast three-dimensional/two-dimensional solar cell simulator featuring conductive boundary and quasi-neutrality approximations. *IEEE T Electron Dev*. 2013;60(2):733-738.
42. Dumbrell R, Juhl MK, Trupke T, Hameiri Z. Extracting metal contact recombination parameters from effective lifetime data 2018;8(6): 1413-1420.
43. McIntosh KR, Sinton RA. Uncertainty in photoconductance lifetime measurements that use an inductive-coil detector. Paper presented at: 23rd European Photovoltaic Solar Energy Conference 2008.
44. Schenk A. Finite-temperature full random-phase approximation model of band gap narrowing for silicon device simulation. *J Appl Phys*. 1998;84(7):3684-3695.
45. Richter A, Glunz SW, Werner F, Schmidt J, Cuevas A. Improved quantitative description of Auger recombination in crystalline silicon. *Phys Rev B*. 2012;86(16):165202-1-165202-14.
46. Klaassen DBM. A unified mobility model for device simulation—I. Model-equations and concentration-dependence. *Solid State Electron*. 1992;35(7):953-959.
47. Pässler R. Semi-empirical descriptions of temperature dependences of band gaps in semiconductors. *Phys Status Solidi B*. 2003;236(3): 710-728.
48. van Sark W, Korte L, Roca F. Physics and Technology of Amorphous-Crystalline Heterostructure Silicon Solar Cells. Springer; 2012.
49. Bivour M, Temmler J, Steinkemper H, Hermle M. Molybdenum and tungsten oxide: High work function wide band gap contact materials for hole selective contacts of silicon solar cells. *Sol Energ Mat sol C*. 2015;142:34-41.
50. Meyer J, Hamwi S, Kröger M, Kowalsky W, Riedl T, Kahn A. Transition metal oxides for organic electronics: Energetics, device physics and applications. *Adv Mater*. 2012;24(40):5408-5427.
51. Greiner MT, Helander MG, Tang W-M, Wang Z-B, Qiu J, Lu Z-H. Universal energy-level alignment of molecules on metal oxides. *Nat Mater*. 2012;11(1):76-81.
52. Bullock J, Hettick M, Geissbühler J, et al. Efficient silicon solar cells with dopant-free asymmetric heterocontacts. *Nat Energy*. 2016;1(3): 1-7.
53. Hummel R. Reflectivity of silver-and aluminium-based alloys for solar reflectors. *Sol Energy*. 1981;27(6):449-455.
54. Holman ZC, de Wolf S, Ballif C. Improving metal reflectors by suppressing surface plasmon polaritons: a priori calculation of the internal reflectance of a solar cell. *Light: Science & Applications*. 2013; 2(10):e106-e106.
55. Holman ZC, Filipič M, Lipovšek B, et al. Parasitic absorption in the rear reflector of a silicon solar cell: Simulation and measurement of the sub-bandgap reflectance for common dielectric/metal reflectors. *Sol Energ Mat Sol C*. 2014;120:426-430.
56. Zhong S, Dreon J, Jeangros Q, et al. Mitigating plasmonic absorption losses at rear electrodes in high-efficiency silicon solar cells using dopant-free contact stacks. *Adv Funct Mater*. 2020;30(5): 1907840-1-1907840-9.
57. Taguchi M, Maruyama E, Tanaka M. Temperature dependence of amorphous/crystalline silicon heterojunction solar cells. *Jpn J Appl Phys*. 2008;47(2R):814-818.
58. Nogay G, Seif JP, Riesen Y, et al. Nanocrystalline silicon carrier collectors for silicon heterojunction solar cells and impact on low-temperature device characteristics. *IEEE J Photovolt*. 2016;6(6):1654-1662.
59. Seif JP, Menda D, Descoedres A, et al. Asymmetric band offsets in silicon heterojunction solar cells: impact on device performance. *J Appl Phys*. 2016;120(5):054501-1-054501-7.
60. Green MA. *Solar Cells: Operating Principles, Technology, and System Applications*. Prentice-Hall; 1982.
61. Green MA. Intrinsic concentration, effective densities of states, and effective mass in silicon. *J Appl Phys*. 1990;67(6):2944-2954.
62. Zhao J, Wang A, Robinson S, Green M. Reduced temperature coefficients for recent high-performance silicon solar cells. *Prog Photovolt Res Appl*. 1994;2(3):221-225.
63. Green MA. Solar cell fill factors: general graph and empirical expressions. *Solid State Electron*. 1981;24(8):788-789.
64. Algara C, Rey-Stolle I. *Handbook of Concentrator Photovoltaic Technology*. John Wiley & Sons; 2016.
65. Luderer C, Messmer C, Hermle M, Bivour M. Transport losses at the TCO/a-Si:H/c-Si heterojunction: Influence of different layers and annealing. *IEEE J Photovolt*. 2020;10(4):952-958.
66. Kane D, Swanson R. Measurement of the emitter saturation current by a contactless photoconductivity decay method. 18th IEEE Photovoltaic Specialists Conference. 1985;578-583.
67. Varache R, Leendertz C, Gueunier-Farret M, Haschke J, Muñoz D, Korte L. Investigation of selective junctions using a newly developed tunnel current model for solar cell applications. *Sol Energ Mat Sol C*. 2015;141:14-23.

SUPPORTING INFORMATION

Additional supporting information may be found in the online version of the article at the publisher's website.

How to cite this article: Le AHT, Dréon J, Michel JI, et al. Temperature-dependent performance of silicon heterojunction solar cells with transition-metal-oxide-based selective contacts. *Prog Photovolt Res Appl*. 2022;30(8): 981-993. doi:[10.1002/pip.3509](https://doi.org/10.1002/pip.3509)